Analysis of Altitude and Ambient Temperature Effects on the Reactivity of Oxidation Catalysts in the Presence of H2

José Ramón Serrano , Pedro Piqueras * , Enrique José Sanchis , Carla Conde

Posted Date: 1 May 2024

doi: 10.20944/preprints202405.0045.v1

Keywords: hydrogen; emissions; altitude; exhaust aftertreatment system; ambient temperature; low temperature; light-off

Article

Analysis of Altitude and Ambient Temperature Effects on the Reactivity of Oxidation Catalysts in the Presence of H_2

José Ramón Serrano, Pedro Piqueras *, Enrique J. Sanchis and Carla Conde

CMT-Clean Mobility & Thermofluids, Universitat Politècnica de València, Camino de Vera s/n, 46022 Valencia, Spain; jrserran@mot.upv.es (J.R.S.); ensanpac@mot.upv.es (E.J.S.); cconcor@upv.edu.es (C.C.)

* Correspondence: pedpicab@upv.edu.es; Tel.: +34-963877650

Abstract: Worldwide emission standards are now required to cover engine operation under extreme ambient conditions, which affect the raw emissions and the efficiency of the exhaust aftertreatment systems. These regulations also target new combustion technologies for decarbonization, such as neat hydrogen (H_2) combustion or dual-fuel strategies, which involve a challenge to the analysis of exhaust aftertreatment systems requirements and performance. This work addresses the impact of high altitude and low ambient temperature conditions on the reactivity of an oxidation catalyst in the presence of H_2. A reaction mechanism is proposed to cover the main conversion paths of CO, HC, and H_2, including the formation and consumption of high-energy surface reaction intermediates. The mechanism has been implemented into a faster-than-real-time reduced-order model for multi-layer washcoat honeycomb catalytic converters. The model was utilized to investigate the effect of H_2 concentration on the reactivity of CO and HC within the catalyst under various operating and ambient conditions. By applying the model and examining the selectivity towards different reaction pathways in the presence of H_2, insights into surface intermediates and reactivity across different cross-sections of the monolith were obtained. This analysis discusses the underlying causes of reactivity changes promoted by H_2 and its relative importance as a function of driving boundary conditions.

Keywords: hydrogen; emissions; altitude; exhaust aftertreatment system; ambient temperature; low temperature; light-off

1. Introduction

Stringent emissions regulations reflect growing societal demands for cleaner and more sustainable transportation [1]. The introduction of Real Driving Emissions (RDE) testing and the Worldwide harmonized Light vehicles Test Cycles (WLTC) within the Worldwide harmonized Light vehicles Test Procedure (WLTP) framework aims to narrow the gap between homologation and real-world emissions of Internal Combustion Engines (ICE) [2]. However, research indicates that vehicles meeting current standards still emit significant pollutants under specific conditions, such as cold starts [3], short trips [4], and scenarios involving high altitudes [5] or extreme ambient temperatures [6]. Current RDE tests establish environmental limits to assess vehicle emissions control in real-world driving scenarios [7]. These tests define two categories: moderate conditions (altitude 0-700 m, temperature 0-30°C) and extended conditions (altitude 700-1300 m, temperature -7 to 35°C) [8]. Furthermore, the upcoming Euro 7 regulations will cover a broader range of driving scenarios [9]. This new regulation predictably proposes to extend the temperature limits to -7°C to 35°C for moderate conditions and increase the maximum altitude to 1600 m. Extended conditions will cover altitudes up to 2200 m and temperatures ranging from -10 to 45°C [10]. This strategy addresses the emission challenges of low cold-start temperatures and high summer temperatures across Europe, reflecting the diversity of driving conditions and climates across the continent [11].

Studies demonstrate that extreme environmental conditions, specifically low temperatures and high altitudes, negatively impact ICE performance and exhaust aftertreatment systems (ATS). The study by Giechaskiel *et al.* [12] revealed that CO, HC, and NOx emissions from a Euro 6d-temp gasoline engine doubled at -10°C compared to mild ambient temperatures during urban driving

 doi:10.20944/preprints202405.0045.v1

scenarios, particularly spiking during cold start conditions. The research by Luján *et al.* [13] showed that low temperatures significantly impacted emissions from a light-duty diesel engine, with CO, HC, and NOx emissions doubling or even tripling during WLTC at -7°C compared to 20°C . Also, research by Bermúdez *et al.* [14] on Euro 4 internal combustion engines and by Suarez-Bertoa *et al.* [15] analyzing road emissions from three Euro 6d-TEMP engines (diesel, gasoline, and hybrid electric gasoline) demonstrated that higher altitudes tend to increase raw emissions of CO and NOx.

In lean ICEs, oxidation catalysts (OC) are essential for reducing pollutants like CO and HC. The efficiency of these catalysts, however, is influenced by environmental conditions. A study by Serrano *et al.* [16], examining a Euro 6d-Temp ICE at various altitudes (0 and 2500 m) and temperatures (20°C and -7°C), reported increased raw emissions of CO and HC and decreased OC efficiency at 2500 m and -7°C. Additionally, increased CO and HC raw emissions at higher altitudes lead to higher inhibitory effects, damaging OC performance. Historical research, including studies by Voltz *et al.* [17] and Oh *et al.* [18], has established that CO and HC presence impairs the oxidation process, decreasing conversion efficiency. Notably, at lower temperatures, the inhibitory effects of CO and HC on oxidation increase [19]. Additionally, research by Lefort *et al.* [20], utilizing various diesel fuels and operational settings with different CO, HC, and NOx levels, indicated that increased CO concentrations lead to higher CO and HC light-off temperatures. However, at elevated temperatures, the inhibition effect on oxidation declined because of decreased chemisorption. These observations underscored the competitive nature of CO [21] and HC [22] against O_2 for binding to active sites and the critical role of surface intermediates.

The presence of H_2 in exhaust gases is unusual in traditional ICEs. Nonetheless, with regulatory shifts favoring the adoption of alternative fuels and technologies to decrease CO_2 emissions, H_2 has emerged as a critical element in transitioning towards more sustainable transportation [23]. This shift encompasses strategies involving H_2 combustion [24] and dual-fuel strategies [25]. Specifically, the dual-fuel H_2 combustion approach has demonstrated substantial gains in fuel efficiency and a general decrease in raw emissions [26]. This enhacement is attributed to the formation of reaction intermediates favoured by the H_2 promotion of hydroxyl radicals on the catalyst surface [27]. However, introducing H_2 as a fuel alters the composition of exhaust gases, impacting the operating conditions for ATS. Consequently, a comprehensive assessment of ATS performance is essential to ensure its effectiveness across various conditions, notably when its efficiency can be affected.

From this background, this work examines the impact of H_2 on an OC under various environmental conditions. A simplified reaction mechanism including the primary conversion paths for CO, HC, and H_2 was implemented into a one-dimensional model for multi-layer washcoat honeycomb catalytic converters [28]. The model was calibrated with data from two sets of experimental tests. First, data from a Euro 6d-Temp Internal Combustion Engine (ICE) coupled with a MEDAS altitude simulator was used, operating at two distinct conditions: sea level (0 m) and 20°C, and an altitude of 2500 m with a temperature of -7°C. This data was used as the basis for calibrating the model in the absence of H_2. To assess the impact of H_2, the calibration process integrated selectivities for various reaction pathways, derived from the simulation of temperature ramp tests conducted on diesel exhaust gases with varying concentrations of H_2. The calibrated model was then used to evaluate how H_2 affects the conversion efficiency of CO and HC under the specified environmental conditions, covering a broad spectrum of H_2 concentrations. Furthermore, the study investigated the reactivity of CO and HC within the catalyst monolith, focusing on the selectivity towards different oxidation pathways. The objective was to understand how H_2 variably influences these reaction pathways in the environmental scenarios studied and to identify the mechanisms behind these differences. This understanding is crucial to optimize OC control in dual-fuel diesel-H_2 ICE under various environmental conditions.

 doi:10.20944/preprints202405.0045.v1

2. Materials and Methods

This study used a combination of experimental and theoretical methods to analyze the effect of H_2 presence in the exhaust gas on the operation of an OC in warm sea-level and high altitude and low-temperature conditions, representative of real driving scenarios.

The initial phase of the study was based on tests conducted by Serrano *et al.* [16] on an HSDI diesel Euro 6d-Temp engine installed in a test bench coupled with the Horiba MEDAS. The MEDAS system, an altitude simulator developed by CMT - Thermofluids & Clean Mobility [29,30], facilitated variable working pressure for the engine based on the designated driving altitude. These tests provided the baseline data to calibrate the reactions that do not involve H_2 in the OC model. In the second part of the study, the model reactions influenced by the presence of H_2 were calibrated using the selectivities of CO and HC to different reaction pathways [31]. After performing the model calibration, a comprehensive analysis was conducted to assess the impact of H_2 on the conversion efficiency and selectivities of CO and HC reactions along the monolith cross-section under both cold altitude and warm sea-level conditions. This analysis covered different molar fractions of H_2 representative of exhaust gases from a dual-fuel H_2-diesel engine. The fractions included 500 ppm and 1000 ppm of H_2, as well as post-injection strategies employing 5000 ppm and 10000 ppm of H_2.

2.1. Experimental Setup

The experimental facility used as a base to conduct the first part of the study consisted of an HSDI diesel Euro 6d-Temp engine for passenger car application, whose detailed characteristics are described in [16]. The engine was installed in a test bench integrated with Horiba MEDAS which can handle altitudes from sea level to 5000 m and ambient temperatures from -15 to 45°C [29]. The ATS comprised a close-coupled OC and a wall-flow particulate filter coated as a selective catalytic reduction system. The characteristics of the OC are listed in Table 1.

Table 1. Characteristics of the oxidation catalyst.

Substrate	Cordierite
Washcoat	Alumina oxide and zeolite
Coating	Pt
Monolith length [mm]	140
Monolith diameter [mm]	120
Channel cross-section	Square
Cell density [cpsi]	400
Cell size [mm]	1.04
Wall thickness [mm]	0.23
Catalytic area [m^2]	3.95

The experiments conducted by Serrano *et al.* [16] were carried out under steady-state conditions, with the engine operating at constant torque and speed until thermal stabilization was achieved, enabling the measurement of CO and HC conversion efficiencies. These tests were guided by the gas inlet temperature and the exhaust gas mass flow of the OC, which were constrained by the two distinct ambient conditions. To establish a baseline for comparison, the conversion efficiency of pollutants was measured at 0 m of altitude and 20°C, referred to as the warm sea-level case. This was then compared to the results obtained at 2500 m of altitude, corresponding to an ambient pressure of 0.747 bar and a temperature of -7°C, referred to as the cold altitude case. To establish the mass flow of exhaust gases, the engine speed was assessed at 1000 rpm, 1250 rpm, and 1500 rpm under warm sea-level conditions. Following this, the speed range was modified for the cold altitude scenario to achieve a comparable exhaust mass flow in both situations. Additionally, the OC inlet gas temperature was controlled within the same range (100 to 300°C) for both cases. The exhaust gas mass flow, catalyst inlet pressure and temperature, along with CO and HC concentrations at the catalyst inlet for both warm sea-level and cold altitude cases, are detailed in Appendix A - Tables A1 and A2.

 doi:10.20944/preprints202405.0045.v1

At each tested point, pollutants were continuously measured according to the specific measurement protocol described in [16]. The results of CO and HC conversion efficiency of the experimental tests for both warm sea-level and cold altitude cases are shown in the conversion efficiency maps in Figure 1, which is analyzed in detail in [16].

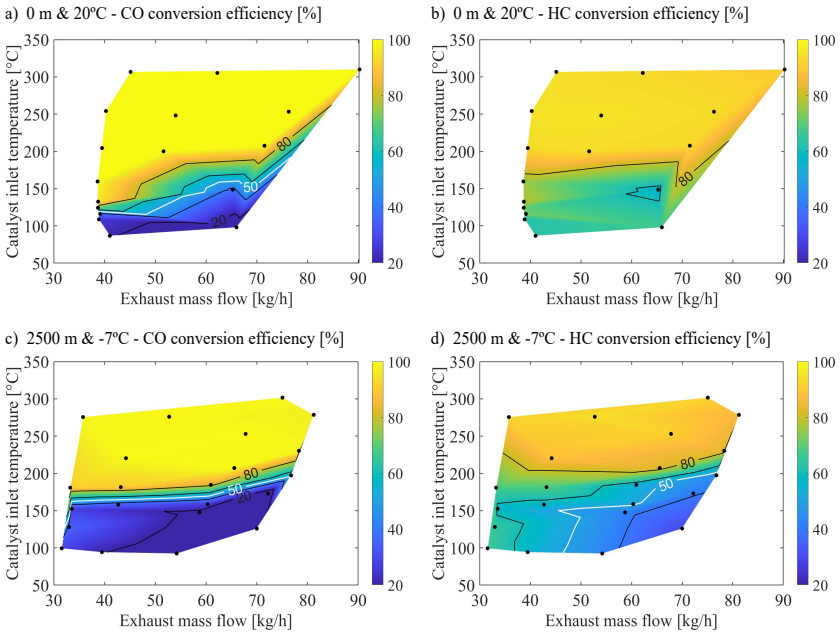

Figure 1. Experimental results for CO and HC conversion efficiency as a function of exhaust mass flow and catalyst inlet temperature for both warm-sea level and cold altitude conditions: (**a**) CO conversion efficiency at 0 m & 20°C; (**b**) HC conversion efficiency at 0 m & 20°C; (**c**) CO conversion efficiency at 2500 m & -7°C; and, (**d**) HC conversion efficiency at 2500 m & -7°C [16].

To conduct the second part of the study, which examines the effect of H_2 on the OC under warm sea-level and cold altitude cases, modeling results from a previous work by Piqueras *et al.* [31] were employed. These results analyzed the selectivity of CO and HC reactions to O_2 and ·OH due to the presence of H_2 using a reduced-order model proposed by Piqueras *et al.* [28]. The selectivities were modeled based on experimental temperature ramp tests carried out by Herreros *et al.* [32]. These tests involved a Pt-coated OC on alumina, which was placed in a tubular furnace in the by-pass of the exhaust line of a single-cylinder diesel engine. The catalyst inlet gas was doped with varying molar fractions of H_2, ranging from 500 to 8000 ppm. The resulting CO and HC selectivities as a function of the temperature and H_2 inlet molar fraction were integrated into the calibration of the catalyst model utilized in this study.

2.2. Catalyst Model

The study employed a flow-through monolith oxidation catalyst model for dual-layer washcoat, as proposed by Piqueras *et al.* [28]. This model is incorporated into VATS, a software developed by CMT-Clean Mobility & Thermofluids, designed to simulate ATS. VATS is coupled with VEMOD, a gas dynamic software utilized for engine simulation [33]. Detailed descriptions of the model for dual-layer washcoat catalysts can be found in [28], which is based on earlier developments focused on deriving explicit solutions for flow transport in catalytic reactors with single-layer washcoats [34,35] from a 1+1D two-phase approach [36]. The model calculates the concentration of chemical species in the bulk gas along the monolith. It includes convective and diffusive transport mechanisms and accounts for chemical reactivity in dual-layer washcoat structures. The model assumes constant flow properties across the monolith inlet and negligible radial temperature gradients, ensuring consistent behavior across all channels [35], as well as quasi-steady incompressible flow [37,38]. The chemical species

 doi:10.20944/preprints202405.0045.v1

conservation equations, corresponding to a single channel bulk gas (Equation 1) and washcoat layers (Equations 2-3) are written as:

$$u_x \frac{\partial c_g}{\partial x} = -S_{s,g} J_{g,wc_1} \tag{1}$$

$$-\sum_{r_{wc_1}} \nu_{r_{wc_1}} R^m_{r_{wc_1}} = S_{s,wc_1} \left(J_{g,wc_1} - J_{wc_1,wc_2} \right) \tag{2}$$

$$-\sum_{r_{wc_2}} \nu_{r_{wc_2}} R^m_{r_{wc_2}} = S_{s,wc_2} J_{wc_1,wc_2} \tag{3}$$

In the equations, subscripts g, wc_1, and wc_2 denote the bulk gas and the two washcoat layers, respectively. The variable u_x indicates the axial velocity of the gas. The term $R^m_{r_{wc_i}}$ quantifies the reaction rate of an m^{th}-order reaction, and $\nu_{r_{wc_i}}$ are the stoichiometric coefficients, with positive values for products and negative values for reactants. Additionally, S_s refers to the specific surfaces of the gas and each substrate layer. The terms J_{g,wc_1} and J_{wc_1,wc_2} describe the fluxes at the interface between the gas and the upper washcoat layer, and between the upper and lower washcoat layers, respectively [28].

The fundamentals of the explicit solver development for chemical species transport lies in the dependence of the interfacial fluxes on the species concentration at every phase, as proposed by Ratnakar *et al.* [38].

An explicit solution is obtained to determine the concentration of the chemical species at the outlet of the monolith according to Equation 4. Constants b and d are functions of specific surfaces, diffusion times, reaction rates and Sherwood numbers, as detailed in [28].

$$c_{g,out} = \frac{\left(d + b c_{g,in}\right) e^{-S_{s,g} b \tau} - d}{b} \tag{4}$$

In parallel to the solution of the chemical species transport, the energy balance in the gas and solid phases is also addressed due to the influence of substrate temperature on reactivity and outlet gas concentration, as detailed in [28].

Regarding the reaction mechanism of the model, which is depicted in Table 2, it involves primary processes in an OC, covering HC adsorption/desorption (R_1 and R_2), CO and HC oxidation with O_2 (R_3 and R_4), and NOx interconversion (R_5 and R_6), detailed in [31]. While these reactions address catalyst behavior with excess O_2, they lack sensitivity to H_2 presence. Introducing ·OH radicals as intermediates captures the influence of H_2. Mhadeshwar and Vlachos [27] proposed a microkinetic scheme highlighting the significance of carboxylic pathway in CO-·OH interaction, modeled by reactions R_8 and R_9. This pathway offers an alternative to direct CO oxidation, involving a two-step reaction route forming ·COOH groups on Pt surface, represented by reaction R_{11}, as detailed in [31]. A similar radical pathway models HC light-off temperature reduction [32] via reaction R_{12}. Despite the oxidative environment, reactions like water gas shift (R_{13} and R_{14}) and steam reforming (R_{15}) are included for comprehensive analysis, despite their minor contribution. The competitive interaction among species is taken into account through the incorporation of an inhibition term, specifically defined for the oxidation of CO and HC (reactions R_3 and R_4 in Table 2). The inhibition term (G_{ox}) was derived using the expression proposed by Voltz *et al.* [17] as detailed in [16].

Finally, Table 2 presents the comprehensive reaction mechanism along with the corresponding rates for each reaction accounted for in every catalyst layer, including kinetic constants (k_i) derived from the Arrhenius equation. Equilibrium constants of the NOx interconversion reaction ($K_{eq,NOx}$) and the water-gas shift reaction ($K_{eq,water}$) are also included, calculated from the thermodynamic data obtained in [39] and [40], respectively.

 doi:10.20944/preprints202405.0045.v1

Table 2. H_2-OC reaction mechanism.

Reaction	Reaction expression rate
Zeolite layer	
$C_nH_m + Zeol \leftrightarrows C_nH_m - Zeol$	$R_1 = k_1 c_{HC}(1-\theta_{HC})$ $R_2 = k_2 \theta_{HC}$
Platinum layer	
$CO + \frac{1}{2}O_2 \rightarrow CO_2$	$R_3 = \frac{k_3}{G_{ox}} c_{CO} c_{O_2}$
$C_nH_m + \left(n + \frac{m}{4}\right)O_2 \rightarrow nCO_2 + \left(\frac{m}{2}\right)H_2O$	$R_4 = \frac{k_4}{G_{ox}} c_{HC} c_{O_2}$
$NO + \frac{1}{2}O_2 \leftrightarrow NO_2$	$R_5 = k_5 c_{O_2} c_{NO}$ $R_6 = \frac{k_5}{K_{eq,NOx}} c_{NO_2}$
$H_2 + \frac{1}{2}O_2 \rightarrow H_2O$	$R_7 = k_7 c_{H_2} c_{O_2}$
$H_2 + O_2 + 2Pt \leftrightarrow 2 \cdot OH - Pt$	$R_8 = k_8 c_{O_2} c_{H_2}(1-\theta_{OH})$ $R_9 = k_9 \theta_{OH}$
$H_2 + 2 \cdot OH - Pt \rightarrow 2H_2O + 2Pt$	$R_{10} = k_{10} c_{H_2} \theta_{OH}$
$CO + 2 \cdot OH - Pt \rightarrow H_2O + CO_2 + 2Pt$	$R_{11} = k_{11} c_{CO} \theta_{OH}$
$C_nH_m + \cdot OH - Pt + \left(\frac{4n+m-1}{4}\right)O_2 \rightarrow nCO_2 + \left(\frac{m+1}{2}\right)H_2O + Pt$	$R_{12} = k_{12} c_{HC} \theta_{OH}$
$CO + H_2O \leftrightarrow CO_2 + H_2$	$R_{13} = k_{13} c_{CO} c_{H_2O}$ $R_{14} = \frac{k_{13}}{K_{eq,water}} c_{CO_2} c_{H_2}$
$C_nH_m + nH_2O \rightarrow nCO + \left(n + \frac{m}{2}\right)H_2$	$R_{15} = k_{15} c_{HC} c_{H_2O}$

3. Results and Discussion

This section discusses the results obtained from modeling the catalyst to assess the reactivity in the presence of H_2 by applying the methodology detailed in Section 2. First, the methodology used and the results obtained to carry out the calibration of the OC model are presented. The analysis of the results obtained after the model calibration was focused on two main parts. Initially, the study examined the reactivity of CO in the OC across various molar fractions of H_2 under warm sea-level and cold high-altitude conditions. Subsequently, the reactivity of HC in the OC under the same conditions was also studied. In both cases, the evolution of the selectivity of CO and HC to $O_2/\cdot OH$ and HC adsorption and the conversion efficiency of both species along the cross-section of the monolith were analyzed.

3.1. Modeling H_2 Effect on Reactivity under Altitude and Sea Level Conditions

The initial phase of the study focused on model calibration to reproduce observed conversion efficiencies for CO and HC during steady-state tests conducted under warm sea level and cold altitude conditions, as referenced in [16] and detailed in Section 2.1. The calibration tests are detailed in Table A1 for warm sea-level conditions (0 m and 20°C), and in Table A2 for cold high-altitude conditions (2500 m and -7°C). Both tables are located in Appendix A.

Due to the absence of H_2 in these tests, calibration was restricted to reactions excluding this species. Specifically, it focused on HC adsorption and desorption (R_1 and R_2), CO oxidation (R_3), and HC oxidation (R_4) reactions, as outlined in Table 2. The calibration of kinetic constants for these reactions considered the effects of thermal transients on oxidation and the equilibrium of adsorption-desorption, as well as the progressive influence of HC accumulation on the reaction rate of adsorption-desorption. This methodology facilitated a steady-state representation at test completion, distinguishing between HC oxidation and adsorption conversion efficiencies under varying environmental conditions.

In this initial part of the calibration, the objective function, defined in Equation 5 and minimized using the simplex search method by Lagarias *et al.* [41], represented the weighted sum of cumulative errors in conversion efficiency (C_{eff}) for CO and HC. It considered the modulus of the error up to each time point (t) for each pollutant species (p), CO and HC, ensuring balanced weighting for both pollutants.

 doi:10.20944/preprints202405.0045.v1

$$\Phi_{OC_{O_2}} = \sum_{\text{test}} \omega_{\text{test}} \left(\sum_t \varepsilon^t_{CO} + \sum_t \varepsilon^t_{HC} \right) \tag{5}$$

$$\varepsilon^t_p = |C_{eff_{p,exp}} - C_{eff_{p,mod}}| \tag{6}$$

Figure 2 presents the modeling results of the steady-state tests under warm sea-level and cold altitude conditions. The comparison of the model results with experimental data, depicted in Figure 1, underscores its efficacy in simulating CO and HC conversion efficiencies with notable accuracy.

The agreement between Figures 2a and 1a validated the ability of the model to capture CO conversion behavior at warm-sea level. The model successfully predicted the low reactivity below 100°C OC inlet temperature. Additionally, it accurately captured the enhancement in CO conversion efficiency and its sensitivity to changes in exhaust mass flow as temperatures increased. Furthermore, the model accurately identified regions achieving 100% CO conversion.

In the context of CO conversion efficiency under cold altitude conditions, as illustrated in Figure 2c, the model reflected the changes in conversion efficiencies caused by modifying environmental conditions. Notably, it reproduced the elevation in CO light-off temperature and the significant reduction in CO conversion efficiency at reduced exhaust mass flows, a trend more pronounced under cold altitude conditions than warm sea-level conditions.

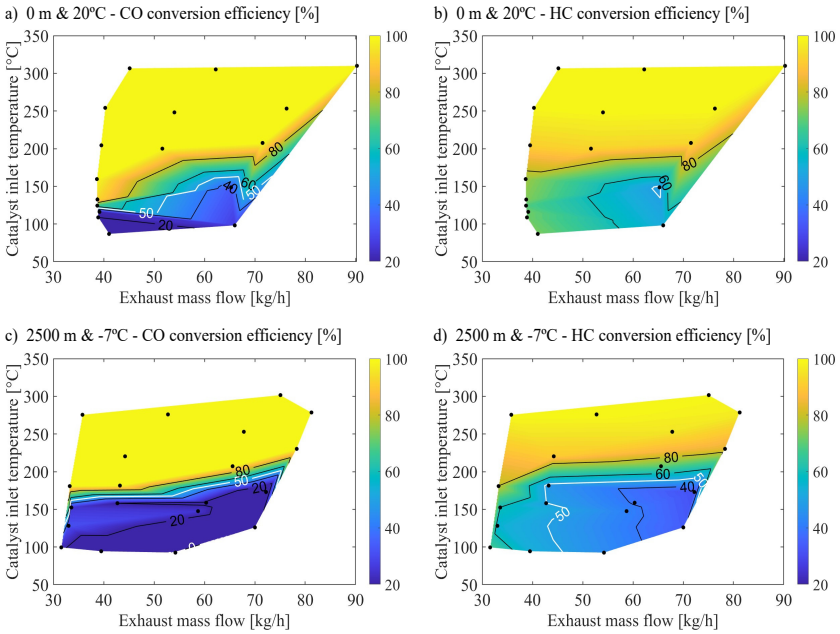

Figure 2. Modeled results for CO and HC conversion efficiency as a function of exhaust mass flow and catalyst inlet temperature: (**a**) CO conversion efficiency at 0 m & 20°C; (**b**) HC conversion efficiency at 0 m & 20°C; (**c**) CO conversion efficiency at 2500 m & -7°C; and, (**d**) HC conversion efficiency at 2500 m & -7°C.

The ability of the model to predict HC conversion efficiency under varying environmental conditions was further validated by comparing Figure 2b,d with their corresponding experimental data of Figure 1b,d. This analysis demonstrates the capacity of the model to capture the influence of exhaust mass flow and OC inlet temperature on HC conversion. Notably, the model accurately predicted the dominance of zeolite adsorption at lower temperatures [16]. Additionally, it captured the dependence of conversion efficiency on both temperature and mass flow rate for oxidation reactions. However, the model predicted a slightly weaker dependence on these factors than the experimental data

 doi:10.20944/preprints202405.0045.v1

The calibrated reactions allow CO and HC elimination prediction across diverse conditions, emphasizing the O_2 oxidation pathway for lean combustion scenarios and accounting for HC accumulation. Nonetheless, these reactions cannot account for the influence of H_2 present in exhaust gases under both warm altitude and sea level conditions, as elaborated in Section 2.1. To address this gap, a targeted calibration of reactions that occur in the presence of H_2 is essential.

Therefore, next phase of calibration focuses on fine-tuning the reactions involving H_2 within the catalyst, specifically targeting reactions R_7 to R_{12} as delineated in Table 2. The goal is to refine the predictive capability of the model regarding the catalytic processes influenced by H_2. A new objective function for this calibration phase was added to reflect the selectivities (S_{p,R_k}) of CO and HC to reactions involving H_2 and O_2 pathways. These selectivities were detailed in a preceding investigation by Piqueras *et al.* [31], which examined the reactivity of an OC across different H_2 concentrations. The objective of this calibration step was to ensure that the elimination of CO and HC occurred in the presence of H_2, following established pathways at each reaction temperature. Selectivity, defined in Equation 7, accounts for the contribution of each reaction (Λ_{p,R_r}) to the conversion of individual species, calculated as the proportion of a change in concentration of a species due to a specific reaction to the total change in that concentration, which is the sum of all reaction contributions.

$$S_{i,R_k} = \frac{\Lambda_{i,R_k}}{\sum_r \Lambda_{i,R_r}} \tag{7}$$

A new error function was formulated based on the selectivities of each reaction, for both the simulation and the reference case, as described in Equation 8.

$$\varepsilon^t_{S_{i,R_k}} = \sum_{test} \left| S^t_{i,R_{k_{OC_{reference}}}} - S^t_{i,R_{k_{OC_{simulation}}}} \right| \tag{8}$$

Equation 9 shows the objective function to calibrate the model in the second part of this study. The second term of this equation refers to the selectivity of CO to the oxidation with O_2 (R_3) and the oxidation with ·OH (R_{11}). It also accounts for the selectivity of HC to the oxidation with O_2 (R_4) and the oxidation with ·OH (R_{12}), without taking into account the adsorption/desorption processes taking place in the zeolite.

$$\begin{aligned} \Phi_{OC_{H_2}} = & \sum_{\text{test}} \omega_{\text{test}} \left(\sum_t \varepsilon^t_{CO} + \sum_t \varepsilon^t_{HC} \right) \\ & + \sum_{\text{test}} \omega_{\text{test}} \left(\sum_{\text{test}} e^t_{S_{CO,R_3}} + \sum_{\text{test}} e^t_{S_{CO,R_{11}}} + \sum_{\text{test}} e^t_{S_{HC,R_4}} + \sum_{\text{test}} e^t_{S_{HC,R_{12}}} \right) \end{aligned} \tag{9}$$

Results of the second part of the calibration are shown in Figure 3, which compares the selectivities for CO and HC oxidation via O_2 or ·OH with those reported by Piqueras *et al.* [31]. The analysis revealed that the presence of H_2 in the exhaust gases yields a closely aligned response between the selectivity of the simulation and the reference.

For CO reactivity, as depicted in Figures 3a,c, the model exhibited a high degree of consistency with the reference data in terms of selectivity. The selectivity towards ·OH, shown in Figure 3c, indicated that at temperatures below 160°C for low H_2 concentrations and below 200°C for high H_2 concentrations, the selectivity was predominantly one, suggesting a preferred pathway. This trend is consistent in both the reference case and the results obtained by the model, with the selectivity being zero in the absence of H_2, indicating that this pathway does not occur in these conditions. Above these temperature thresholds, introducing H_2 led to a decrease in CO selectivity from ·OH to the O_2 oxidation pathway.

 doi:10.20944/preprints202405.0045.v1

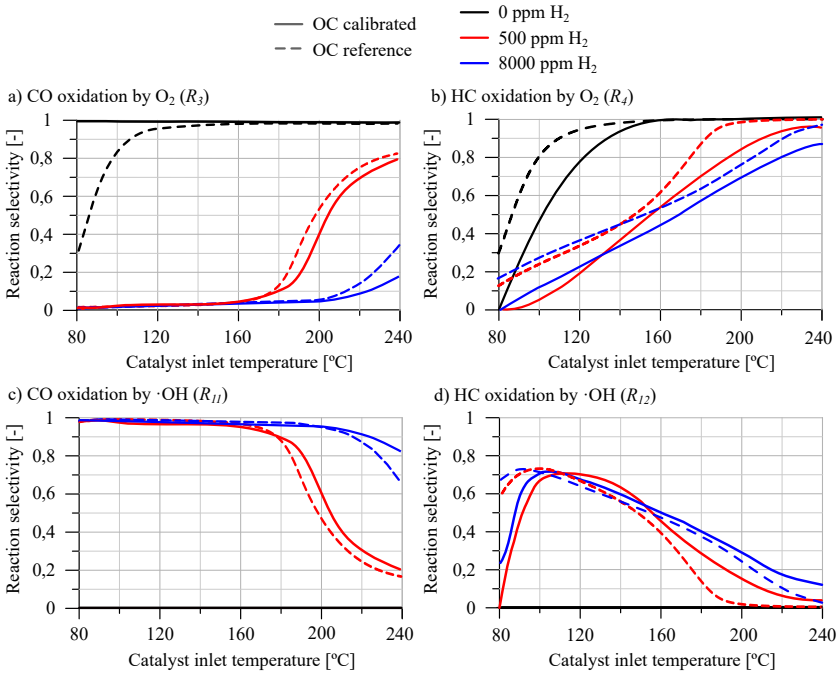

Figure 3. CO and HC selectivity to O_2 and ·OH in OC calibrated and OC reference: (**a**) CO oxidation by O_2; (**b**) HC oxidation by O_2; (**c**) CO oxidation by ·OH; and, (**d**) HC oxidation by ·OH.

Regarding the selectivity of HC oxidation, as depicted in Figure 3b,d, it showed the same type of trend as observed with CO upon the introduction of H_2. However, it did not reach the selectivity levels for the ·OH pathway observed in CO. The influence of H_2 on HC conversion is weaker at low temperatures. While selectivity of ·OH pathway decreases with lower temperature, this decrease is more gradual and less affected by H_2 concentration than for CO. Notably, the presence of adsorption reactions, which are significant under low-temperature conditions, means that the sum of selectivities at low temperatures for oxidation reactions does not total one, indicating that adsorption is an important reaction pathway at low temperature, especially in the absence of H_2.

As a result of this calibration, the kinetic constants collected in Table A3 - Appendix B were obtained. These constants include the activation energies and pre-exponential factors of the reactions involved and the accumulation capacity of HC and ·OH in the catalyst.

Following the calibration of the model to assess environmental changes and the reaction pathways of CO and HC with O_2 and H_2, these subsections examine the influence of H_2 presence on the CO and HC conversion efficiency in both cold altitude and warm sea level conditions. The analysis involved simulating specific experimental conditions described in Section 2.1, which were also employed in the first calibration phase of the model. These simulations incorporated varying mole fractions of H_2, namely 500, 1000, 5000, and 10000 ppm, in the gas mixture at the inlet of the OC.

3.2. CO Reactivity Analysis

For the CO case, Figure 4 shows the percentage increase in CO conversion efficiency relative to the baseline results shown in Figure 2a under warm-sea level conditions, as a function of exhaust mass flow and catalyst inlet temperature. This analysis encompasses the introduction of 500, 1000, 5000, and 10000 ppm of H_2 into the catalyst inlet gas, as detailed in Section 2.

 doi:10.20944/preprints202405.0045.v1

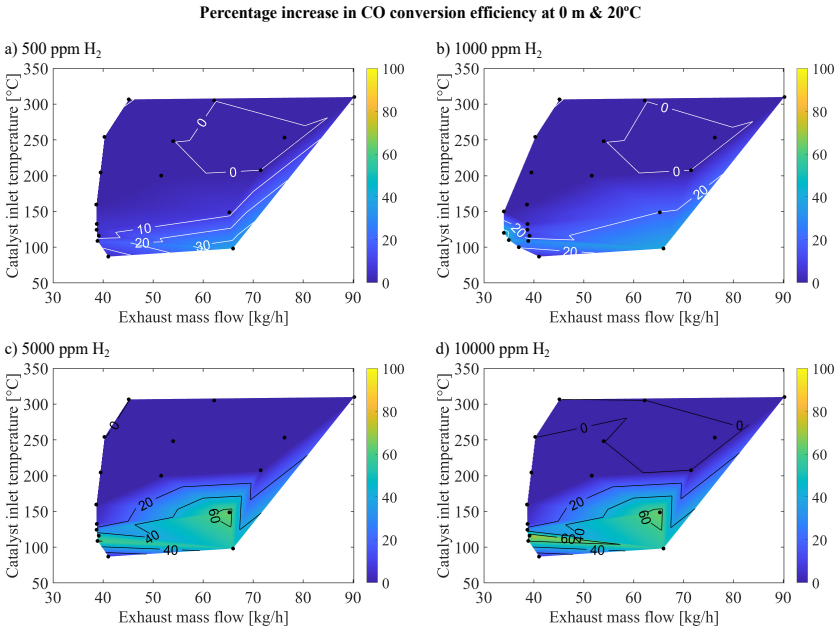

Figure 4. Increase in CO conversion efficiency at 0 m & 20°C as a function of the exhaust mass flow and catalyst inlet temperature for different H_2 inlet molar fractions: (**a**) 500 ppm H_2; (**b**) 1000 ppm H_2; (**c**) 5000 ppm H_2; and, (**d**) 10000 ppm H_2.

The findings indicated an enhancement in CO reactivity with increasing molar fractions of H_2, particularly evident within the low-temperature range under low flow conditions (around 100°C and 35-50 kg/h). This effect extended to higher temperatures as conditions transitioned to higher flow rates (around 150°C with 60-70 kg/h). The improvement in conversion efficiency was most pronounced in the operating points with notably low conversion efficiency in the absence of H_2. These points were characterized by elevated CO concentrations and temperatures insufficient to facilitate oxidation reactions with O_2, as shown in Table A1 in Appendix A.

The improvement in CO conversion efficiency consistently increased up to the introduction of 5000 ppm of H_2, resulting in a significant improvement of over 60% at approximately 150°C and an exhaust mass flow of 65 kg/h. This substantial increase differed from the 20% improvement observed at 1000 ppm of H_2 and less than 10% improvement at 500 ppm of H_2, accompanied by an expansion of the enhanced region to higher temperatures. However, the addition of 10000 ppm of H_2 did not lead to a discernible improvement in reactivity beyond that achieved with 5000 ppm of H_2, with the enhancement stabilized at 60%. This trend indicated a saturation point beyond which further increases in H_2 concentration did not significantly impact reactivity.

The effect of introducing H_2 on improving CO conversion efficiency was also observed under cold altitude conditions. Figure 5 shows the percentage increase in CO conversion efficiency relative to baseline results shown in Figure 2c, considering cold altitude scenarios as influenced by exhaust mass flow and catalyst inlet temperature. Similar to the previous scenario, the same molar fractions of H_2 were introduced into the catalyst inlet gas: 500 ppm, 1000 ppm, 5000 ppm, and 10000 ppm. An enhancement band was observed at 150°C in the low-to-mid mass flow range (30-60 kg/h) for the cases of 1000, 5000 and 10000 ppm of H_2. Introducing 10000 ppm H_2 further extends this band to the highest mass flow rates (70-80 kg/h). This differs from the warm sea-level case, where enhancement occurred at lower temperatures and mass flows (around 100°C and 35-50 kg/h) and at 150°C within the mid-mass flow region with high H_2 molar fractions.

 doi:10.20944/preprints202405.0045.v1

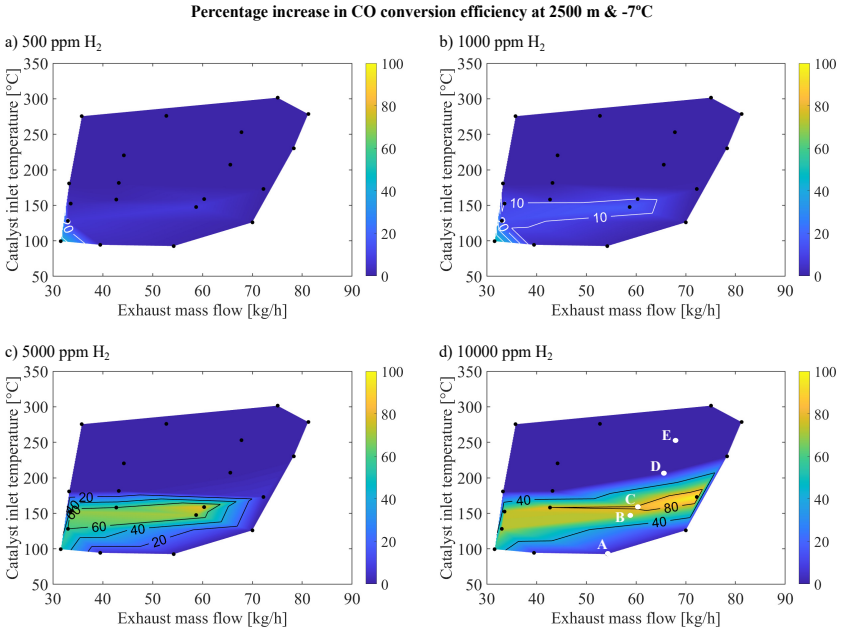

Figure 5. Increase in CO conversion efficiency at 2500 m & -7°C as a function of the exhaust mass flow and catalyst inlet temperature for different H_2 inlet molar fractions: (**a**) 500 ppm H_2; (**b**) 1000 ppm H_2; (**c**) 5000 ppm H_2; and, (**d**) 10000 ppm H_2.

This difference in the increase of CO conversion efficiency profiles was primarily attributed to high CO raw concentration in cold altitude conditions (see Table A2 in Appendix A). This limited the effectiveness of H_2 in enhancing CO reactivity. At lower molar fractions of H_2, such as 500 ppm, the enhancement in conversion efficiency was minimal and limited to regions with low exhaust mass flow and temperature, where the concentration of CO and inhibition was reduced. However, as H_2 molar fraction increased, the enhancement region became more distinct and shifted towards higher exhaust mass flows, highlighting the role of the ·OH reaction pathway and the decrease in inhibition caused by CO consumption. Higher H_2 molar fractions made this effect increasingly apparent. Unlike warm-sea level conditions, high molar fractions of H_2 did not lead to saturation effects in cold altitude conditions in every operating point due to the inherently lower initial reactivity of the catalyst in the absence of H_2. Therefore, significantly greater reactivity was observed when H_2 molar fraction was increased from 5000 to 10000 ppm, especially in areas of high mass flow, which were highly affected by inhibition.

To elucidate the improvement in CO reactivity observed in the regions depicted in Figures 4 and 5 and to understand the variability in the response to H_2 introduction across different operating points. The analysis was initiated by assessing the axial distribution of conversion efficiency throughout the catalyst. This involved identifying the cross-sectional areas of the OC that exhibit the highest reactivity at each operating point, as well as those areas most affected by the introduction of H_2. For this purpose, three sections along the length of the monolith have been selected. First, the catalyst inlet cross-section corresponds to 4.66 mm from the inlet of the monolith. Then, the middle cross-section was 69.99 mm, and the outlet cross-section was 135.34 mm. The study prioritizes the cold altitude case for a more detailed examination, given its more notable increase in reactivity attributed to higher levels of inhibition. Table 3 presents points A-E from Figure 5, representing different operating points of the region where a significant increase in reactivity is noted upon introducing H_2 in the inlet gas mixture, arranged in increasing order by inlet gas temperature and exhaust mass flow to the OC.

 doi:10.20944/preprints202405.0045.v1

Table 3. Selected points for 2500 m & -7°C conditions.

Point	Exhaust mass flow [kg/h]	OC inlet temperature [°C]	CO inlet molar fraction [ppm]	HC inlet molar fraction [ppm]
A	54.22	92.52	1194	838
B	58.72	147.59	616	257
C	60.33	158.77	461	268
D	65.58	207.22	308	175
E	67.81	252.96	222	97

Thus, Figure 6 presents the axial distribution of CO conversion efficiency along the monolith length for points A-E as outlined in Table 3. Each subplot within this Figure corresponds to a different H_2 molar fraction in the catalyst inlet gas. The results for 0 ppm of H_2 shown in Figure 6a, revealed three distinct trends across the five operational points presented. At operating point A, no reactivity was observed across any section of the monolith due to the low inlet gas temperature (92.52°C) and very high CO molar fraction (1194 ppm), resulting in significant inhibition. Points B and C exhibited higher inlet gas temperatures and high CO molar fractions (616 ppm and 461 ppm, respectively) but were lower than point A, indicating OC inhibition. However, the temperature facilitated the reaction of CO with O_2, resulting in heightened reactivity in the monolith cross-sections. As CO started to react at the inlet region of the monolith, its concentration decreased, thereby reducing inhibition in subsequent regions and enhancing overall reactivity along the monolith. In these scenarios, the entire length of the monolith contributed to the reaction, and an expanded catalyst volume would enhance CO conversion efficiency, contrasting with point A. Finally, points D and E, characterized by high inlet gas temperatures and low CO concentrations (with low inhibition), demonstrated conversion efficiencies near 100%, with most reactivity occurring at the inlet cross-section of the monolith.

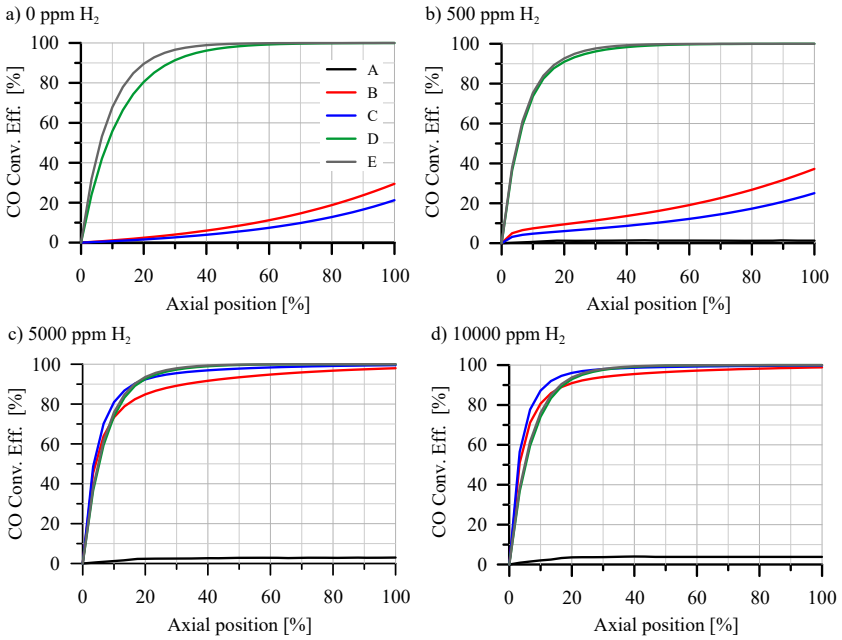

Figure 6. Axial distribution of CO conversion efficiency with different H_2 concentrations for 2500 m & -7°C and points A, B, C, D and E from Table 3: (**a**) 0 ppm H_2; (**b**) 500 ppm H_2; (**d**) 5000 ppm H_2; and, (**d**) 10000 ppm H_2.

Upon introducing 500 ppm of H_2, as shown in Figure 6b, the conversion efficiency results were largely consistent with the 0 ppm of H_2 scenario, with only minor differences. Notably, at points B and C, there was a marginal increase in conversion efficiency in the initial cross-section of the monolith, which exhibited higher local conversion efficiency than subsequent sections. This indicated

 doi:10.20944/preprints202405.0045.v1

an enhanced conversion efficiency in the initial zone, attributed to new reaction pathways facilitated by the presence of H_2, particularly through the formation of ·OH groups on the surface. At this relatively low H_2 concentration, the generation of these surface groups was limited, resulting in only a modest reactivity increase at the monolith inlet. Points D and E also experienced a boost in reactivity from the H_2 presence at the inlet, with point D showing slightly higher reactivity due to the additional H_2, which offsets the lower inlet temperature. This resulted in better conversion efficiency for point D compared to point E, due to its lower inlet mass flow and longer residence time. However, since both points already achieved near 100% conversion efficiency, no significant improvement was noted in the conversion efficiency increase map (Figure 5a). For point A, the presence of H_2 fails to enhance conversion efficiency due to the inlet temperature being too low for reactivity through the new reaction pathway.

The enhancement effects were more pronounced when the H_2 molar fraction was increased to 5000 and 10000 ppm of H_2, as illustrated in Figure 6c,d. At points B and C, the increase in reactivity resulting from the high molar fraction of H_2 led to greater availability of ·OH groups at the monolith inlet, consequently increasing the conversion efficiency to near 100% in these inlet regions. For operating points D and E, the enhanced reactivity improved conversion efficiency in the inlet region, but only marginally, as these points already face limitations due to mass transfer rather than reactivity. The superior reactivity of point C, coupled with its lower inlet flow, allows for higher residence time and conversion efficiency at the inlet compared to points D and E. Furthermore, the elevated availability of ·OH groups with this high H_2 concentration boosts the reactivity at the inlet for operating point A. However, this increase in conversion efficiency was modest due to the low temperature, which does not sufficiently reduce CO concentration to overcome inhibition. Consequently, despite this initial increase, the conversion efficiency throughout the rest of the monolith remained negligible due to the persistent inhibition and low gas temperature.

The findings depicted in Figure 6 demonstrated that H_2 predominantly influences the inlet cross-section of the monolith, with the observed variations in reactivity in subsequent sections resulting from alterations in CO concentration initiated in these inlet cross-sections. To understand why the impact of H_2 presence was primarily at the inlet of the monolith, it is crucial to examine the selectivity of CO reactions with O_2 and ·OH across different operating points and cross-sections of the monolith. Figure 7 illustrates the selectivity of CO towards ·OH in the context of cold altitude conditions with 500 ppm of H_2 (Figures 5a,b) and 10000 ppm of H_2 (Figures 5c,d), for the inlet and medium cross-sections of the monolith.

The reactivity of CO with ·OH varied significantly between the inlet and middle cross-sections. Notably, the selectivity towards CO with ·OH was considerably higher in the inlet cross-section of the monolith for 500 ppm and 10000 ppm of H_2, approaching a value of 1 for most operating points, except in areas showing the most significant increases in conversion efficiency. This selectivity sharply declined along the monolith length, with much lower values in the middle cross-sections, reaching its peak at approximately 0.6 for 500 ppm of H_2 and 0.8 for 10000 ppm of H_2 introduced into the inlet gas. Interestingly, these peaks in selectivity occurred in regions with minimal increases in conversion efficiency. The areas of high selectivity in the middle cross-section aligned with areas of low temperature where there was no reactivity (point A) and, to a lesser degree, with areas of high temperature where conversion efficiency was already elevated without H_2 (points D and E). In both scenarios, reactivity in these areas remained low due to unfavourable conditions that avoid oxidation (point A) or oxidation has already occurred in the inlet cross-section, leaving no residual CO to react (points D and E). This selectivity pattern may seem counterintuitive since the areas with the most pronounced improvements in conversion efficiency, namely points B and C, upon H_2 introduction, appeared least affected by the CO with ·OH reaction pathway. Moreover, the selectivity for this reaction was more significant with 500 ppm of H_2 than with 10000 ppm since, in the latter case, the improvement is much more substantial, but the selectivity is significantly lower.

 doi:10.20944/preprints202405.0045.v1

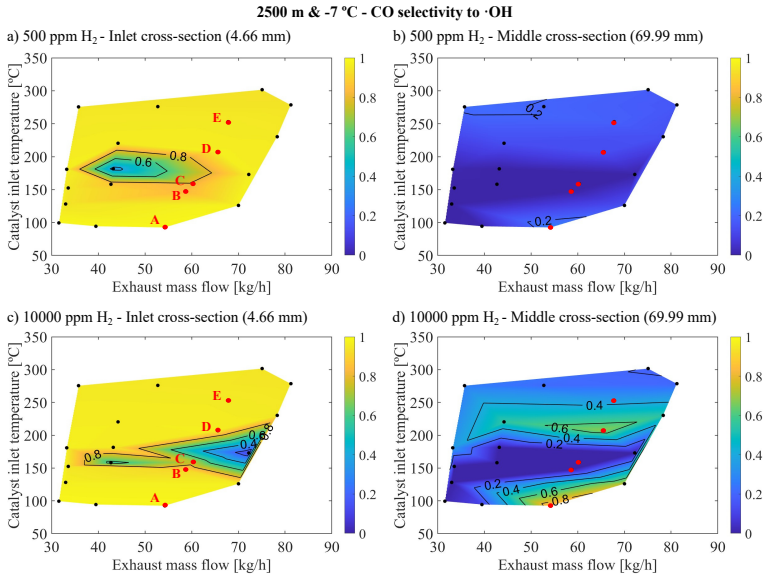

Figure 7. Axial distribution of CO selectivity to ·OH along the cross-section of the monolith at 2500 m & -7°C as a function of the exhaust mass flow and catalyst inlet temperature for 500 and 10000 ppm H_2: (**a**) 500 ppm H_2 - Inlet cross-section; (**b**) 500 ppm H_2 - Middle cross-section; (**c**) 10000 ppm H_2 - Inlet cross-section; and, (**d**) 10000 ppm H_2 - Middle cross-section.

This seemingly contradictory behavior can be elucidated by examining the interplay between oxidation reactions and inhibition dynamics, alongside ·OH coverage, as demonstrated in Figure 8. This figure illustrates ·OH coverage at both 500 and 10000 ppm of O_2, focusing on the inlet and middle cross-sections of the monolith under cold altitude conditions. At points D and E, the variation in CO concentration was less pronounced compared to points B and C, attributed to their lower initial CO concentrations. This facilitated the replacement of CO oxidation with O_2 by oxidation with ·OH, enabled by the relative abundance of H_2, even at 500 ppm, which allowed for significant·OH coverage.

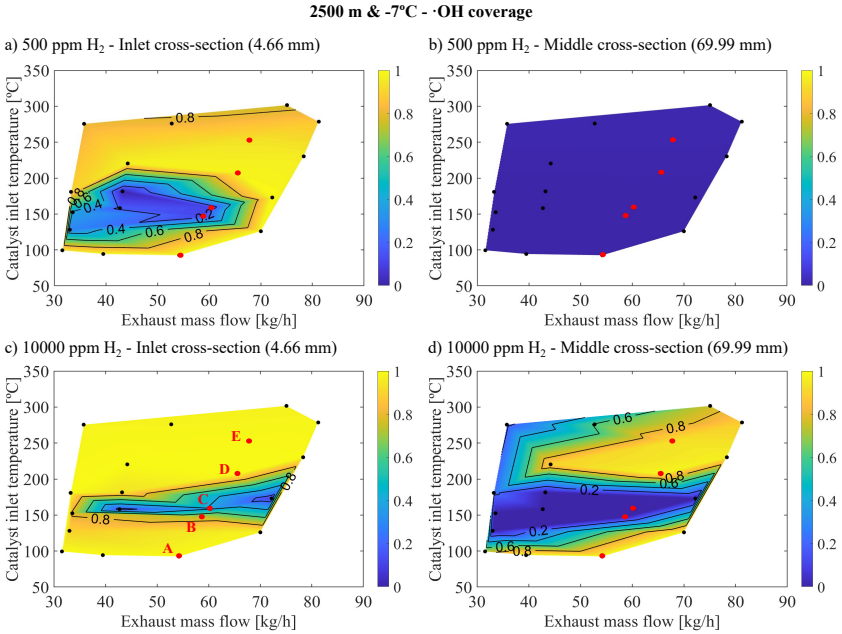

Figure 8. Axial distribution of ·OH coverage along the cross-section of the monolith at 2500 m & -7°C as a function of the exhaust mass flow and catalyst inlet temperature for 500 ppm and 10000 ppm H_2: (**a**) 500 ppm H_2 - Inlet cross-section; (**b**) 500 ppm H_2 - Middle cross-section; (**c**) 10000 ppm H_2 - Inlet cross-section; and, (**d**) 10000 ppm H_2 - Middle cross-section.

 doi:10.20944/preprints202405.0045.v1

However, at points B and C, which had higher initial CO concentrations, the introduction of 500 ppm of O_2 enhanced CO reactivity via the ·OH pathway, as evidenced by observed increases in conversion efficiency and selectivity. Yet, this H_2 concentration was insufficient to sustain high ·OH coverages, limiting the reaction rate, particularly in the inlet cross-section as shown in Figure 8a, which is crucial for overall reactivity. With 10000 ppm of H_2, the ability to generate and maintain ·OH coverage improved significantly in the inlet section (Figure 8c), leading to a substantial reduction in CO concentration and decreased inhibition, thus facilitating oxidation via the O_2 pathway. This resulted in high activity but low selectivity for the ·OH reaction.

After analyzing all cases, it was found that there is a significant correlation between the coverage of ·OH and selectivity, confirming that in operating points where conversion efficiency improved, most notably under altitude conditions, the reaction rate was constrained by the capability to stabilize ·OH coverage. This elucidates why no saturation in conversion efficiency enhancement was observed with higher H_2 molar fractions at altitude, as the increased H_2 molar fraction boosted the ·OH coverage in the most positively affected operating points. With 10000 ppm of H_2, selectivity saturation had not been reached indicating a higher selectivity for reactions with O_2 but the reaction with ·OH effectively reduced CO enough to decrease inhibition, thereby enabling reactivity with O_2 and achieving conversion efficiency saturation.

Moreover, at the highest temperature points, ·OH coverage neared saturation at the inlet (approaching saturation in intermediate regions) due to diminished reactivity from lower CO concentrations at the inlet. These areas did not benefit from further H_2 introduction. Conversely, low-temperature regions also reached ·OH saturation, but the prevailing temperatures were too low for significant reactivity, hence not benefiting from increased H_2 concentration. Therefore, it is evident that certain operating points do not gain from H_2 introduction, whereas those that do require higher H_2 molar fractions for cold altitude conditions compared to warm sea level conditions. This is mainly due to the higher CO concentrations in these conditions necessitating higher H_2 mole fractions to stabilize sufficient ·OH coverage to guarantee the elimination of CO in this way. Notably, ·OH coverages decrease abruptly along the channel in the axial direction, indicating that the presence of H_2 primarily enhances reactivity in the inlet sections. This localized improvement is partially attributable to the reduction in the inhibition of oxidation with O_2. Furthermore, this reduction in inhibition is the principal factor behind the reactivity enhancement in downstream regions, as evidenced by the low selectivity of the ·OH reaction pathway (Figure 7b,d), which is a consequence of the limited ·OH coverage (Figure 8b,d).

3.3. HC Reactivity Analysis

In the analysis of the impact of H_2 on HC reactivity, Figure 9 shows an improvement in HC conversion efficiency under warm sea-level and cold altitude scenarios. This figure illustrates the percentage increase in HC conversion efficiency based on the mass flow rate of exhaust gas and the inlet temperature to the OC, particularly at high molar fractions of H_2 (5000 and 10000 ppm) in the exhaust gas for warm-sea level and cold altitude cases. It is observed that the most significant enhancements in HC conversion efficiency induced by H_2 corresponded with the conditions that are also most affected by H_2 in terms of CO conversion efficiency, specifically at temperatures around 140°C - 150°C and an exhaust mass flow of 60 to 65 kg/h. However, in the case of HC, this improvement was less significant, as it aligned with zones where adsorption by reaction R_1 from Table 2 was dominant in the absence of H_2. In this area, oxidation with O_2 by reaction R_4 was not yet significant, but already showed moderate HC conversion efficiencies, as shown in Figure 2b,d.

 doi:10.20944/preprints202405.0045.v1

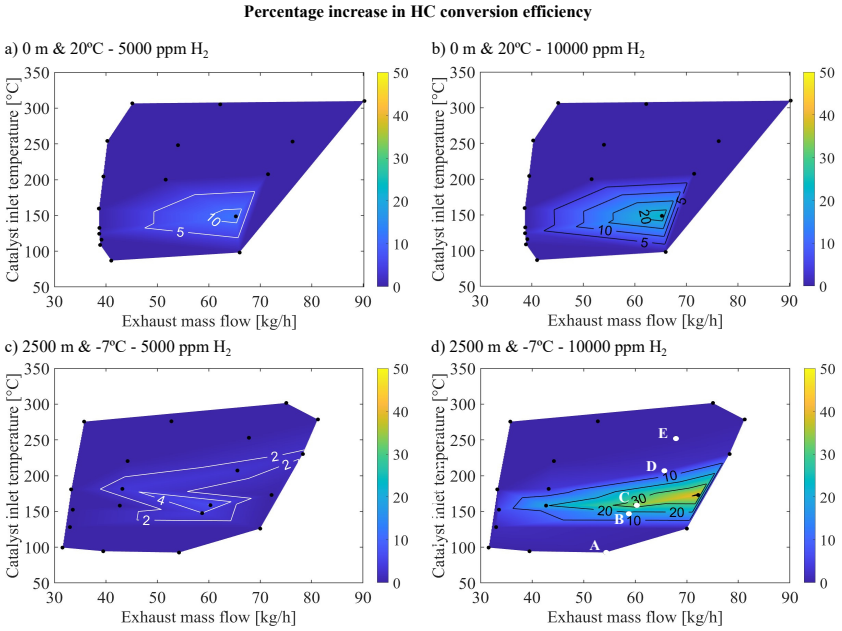

Figure 9. Increase in HC conversion efficiency at 0 m & 20°C and 2500 m & -7°C as a function of the exhaust mass flow and catalyst inlet temperature for different H_2 inlet molar fractions: (**a**) 0 m & 20°C - 5000 ppm H_2; (**b**) 0 m & 20°C - 10000 ppm H_2; (**c**) 2500 m & -7°C - 5000 ppm H_2; and, (**d**) 2500 m & -7°C - 10000 ppm H_2.

Moreover, introducing H_2 gradually increased reactivity under warm sea-level environmental conditions as the concentration of H_2 rises. This was manifested by the fact that introducing 5000 ppm H_2 (Figure 9a) led to maximum improvements of around 10% while introducing 10000 ppm of H_2 resulted in a maximum improvement exceeding 20%. On the other hand, in cold altitude conditions, a significant enhancement in reactivity only occurred with the introduction of 10000 ppm of H_2, as shown in Figure 9d, with conversion efficiency improvements exceeding 30% at point B, whereas introducing 5000 ppm (Figure 9c) yields only minimal changes (maximum improvement of around 5%).

This phenomenon of improvement and the varying behavior between different altitude conditions can be attributed to two complementary factors. Firstly, increased reactivity was facilitated by the reaction pathway between HC and ·OH, following the reaction R_{12} detailed in Table 2. Given the inherently lower reactivity of HC, significant coverage of $\cdot OH$ was required, requiring higher concentrations of H_2. Secondly, greater efficiency in the CO conversion reaction reduced inhibition by this species, facilitating the oxidation of HC with O_2 [16].

In cold altitude conditions, as depicted in Figure 9c,d, an improvement in reactivity only occurred in the presence of 10000 ppm of H_2. Under these conditions, ·OH coverage reached significant levels at the catalyst inlet, as illustrated in Figure 8c, indicating an excess of this intermediary that facilitates the R_4 reaction. Less notably, this phenomenon also occurred at warm-sea level, where HC reactivity increased more gradually because lower amounts of CO at the catalyst inlet required less H_2 to stabilize the necessary ·OH groups.

Finally, the fact that the improvement in the efficiency of the HC reaction was more moderate compared to that of CO is because not only an increase in reactivity but also a change in the adsorption pathway is taking place (R_1) to that of oxidation, both with ·OH (R_{14}) and with O_2 (R_4) (the latter due to the reduction in inhibition). This replacement of one reaction pathway by another was reflected in the global selectivity (integrated across all conditions) of the R_1 reaction, depicted in Figure 10 for warm sea-level conditions with 0 ppm of H_2 (plot a) and with 10000 ppm of H_2 (plot b), and for cold altitude conditions with 0 ppm of H_2 (plot c) and with 10000 ppm of H_2 (plot d).

 doi:10.20944/preprints202405.0045.v1

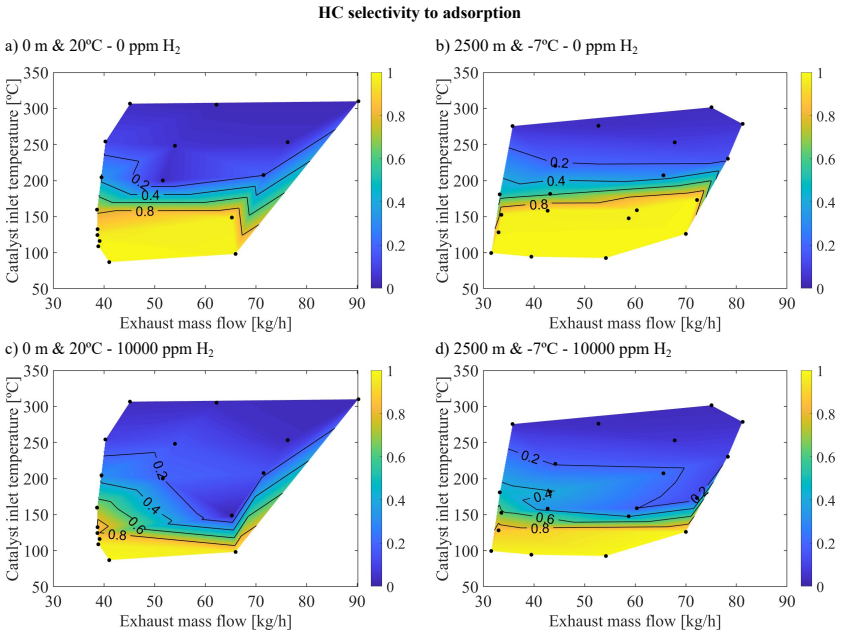

Figure 10. HC selectivity to adsorption as a function of the exhaust mass flow and catalyst inlet temperature for 0 and 10000 ppm of H_2 at different ambient conditions: (**a**) 0 ppm H_2 - 0 m & 20°C; (**b**) 0 ppm H_2 - 2500 m & -7°C; (**c**) 10000 ppm H_2 - 0 m & 20°; and, (**d**) 10000 ppm H_2 - 2500 m & -7°.

The analysis of Figure 10 showed a decrease in the selectivity for adsorption in HC upon the introduction of H_2, with this reaction accounting for 100% of the reactivity when H_2 is not introduced in regions where improvements occur upon its introduction, and also in colder regions. However, this reaction becomes irrelevant for both environmental conditions once the light-off temperature for the R_4 reaction is reached. When 10000 ppm of H_2 was introduced, the selectivity for the R_1 reaction significantly decreased in the area with temperatures around 140 - 150°C and exhaust mass flow of 60 to 65 kg/h, falling from 100% with 0 ppm of H_2 in both environmental conditions to 2% with 10000 ppm of H_2 for the warm sea-level case and to 39% for the cold altitude case. This replacement of one reaction pathway by another is the most significant phenomenon related to the effect of H_2 on the reactivity of HC in these conditions, not implying a particularly relevant change in the overall conversion efficiency of the HC into the OC.

4. Conclusions

In this work, the reactivity of an OC in the presence of H_2 under high altitude and low-temperature conditions has been investigated. Employing a combined approach utilizing both experimental and modeling techniques, the research extended the reaction mechanism to include alternative oxidation pathways based on the formation of ·OH at the active sites of the catalyst. This reaction mechanism was incorporated into a dual-layer washcoat catalyst model to assess the impact of varying H_2 molar fractions on CO and HC reactivity. The robustness of the model was validated against experimental data, accurately reflecting CO and HC conversion efficiencies across various environmental conditions. Introducing H_2 notably enhanced CO conversion efficiencies, especially at specific temperature ranges in different conditions. At sea level, an optimal H_2 concentration of 5000 ppm was identified, beyond which no further benefits were observed. However, in cold altitude conditions, improvements were evident even with 10000 ppm of H_2. Detailed analysis revealed that the greatest enhancement in reactivity due to H_2 occurred in the inlet regions of the monolith, primarily attributed to reactions with ·OH groups. Additionally, a significant portion of the reactivity comes from the O_2 pathway, facilitated by the reduction in CO concentration resulting from the ·OH pathway. In the case of HC, the lower selectivity of ·OH for this species, combined with its higher reactivity at low temperatures, results in a

 doi:10.20944/preprints202405.0045.v1

less pronounced improvement in HC conversion efficiency upon introducing H_2. This improvement also necessitates higher H_2 molar fractions at the inlet.

Consequently, the impact of H_2 concentration on conversion efficiency is closely related to operational and environmental factors. Extremely low-temperature points, below 100°C, do not see benefits from H_2-induced reactivity enhancement. However, points with higher temperatures and moderate CO concentrations do benefit, with warmer sea-level conditions requiring lower H_2 molar fractions compared to colder altitude conditions. Thus, it's advisable to adjust H_2 levels in the exhaust based on operating conditions and altitude, avoiding its presence in low-temperature conditions where it's ineffective and increasing it in colder altitudes compared to warmer sea-level conditions.

Author Contributions: Conceptualization, J.R.S. and P.P.; Methodology, P.P. and C.C.; Software, E.J.S. and C.C.; Formal analysis, P.P. and E.J.S.; Investigation, J.R.S., P.P., E.J.S. and C.C.; Resources, J.R.S.; Writing—original draft preparation, P.P., E.J.S. and C.C.; Writing—review and editing, J.R.S., P.P., E.J.S. and C.C.; Supervision, J.R.S. and P.P.; Project administration, J.R.S; Funding acquisition, J.R.S. All authors have read and agreed to the published version of the manuscript.

Funding: This research has been supported by Grant PID2020-114289RB-I00 funded by the Spanish Ministerio de Ciencia e Innovación, Agencia Estatal de Investigación (MCIN/AEI/10.13039/501100011033). Additionally, C. Conde thanks PhD funding from Universitat Politécnica de Valéncia through grant FPI-2022-S2-49099, which is supported by project CIPROM/2021/061 funded by Generalitat Valenciana.

Conflicts of Interest: The authors declare no conflict of interest.

Abbreviations

The following abbreviations are used in this manuscript:

Acronyms	
1D	One dimensional
ATS	Aftertreatment system
ICE	Internal Combustion Engine
MEDAS	Multifunctional Efficient Dynamic Altitude Simulator
OC	Oxidation Catalyst
RDE	Real Driving Emissions
SCRf	Wall-flow articulate Filter with Selective Catalytic Reduction
WLTC	Worldwide Harmonized Light vehicle & Test Cycle
WLTP	Worldwide Harmonized Light vehicle Test Procedure
Latin Letters	
b	Constant in concentration solution
c	Concentration
C_{eff}	Conversion efficiency
d	Constant in concentration solution
e	Relative cumulative error
G_{ox}	Inhibition term
J	Interfacial flux
k	Arrhenius kinetic constant
$K_{eq,NOx}$	NOx interconversion reaction equilibrium constant
$K_{eq,water}$	Water gas shift reaction equilibrium constant
R	Reaction rate
S	Selectivity
S_s	Specific surface
t	Time
T	Temperature
u	Velocity
wc	Washcoat
x	Axial direction
$Zeol$	Zeolite

 doi:10.20944/preprints202405.0045.v1

Greek letters

Δ	Variation
ε	Modulus of conversion efficiency error
Λ	Contribution
Φ	Objective function
ν	Stoichiometric coefficient
τ	Residence time
θ	Surface coverage
ω	Weight coefficient

Subscripts

a	Axial
exp	Experimental
g	gas
i	Phase (g, wc_1, wc_2)
in	Inlet
H_2	Referred to second part of the calibration procedure
k	Index
mod	Modeled
m	Number of H atoms in HC species
n	Number of C atoms in HC species
out	Outlet
O_2	Referred to first part of the calibration procedure
p	Chemical species
w	Wall
wc	Washcoat

Superscript

m	Reaction order
t	Time

Appendix A

This appendix includes the input data to the catalyst model for the environmental conditions studied: 0 m & 20°C in Table A1, and 2500 m & -7°C in Table A2.

Table A1. Input data for 0 m & 20°C.

Engine speed [rpm]	OC inlet pressure [bar]	Exhaust gas mass flow [kg/h]	OC inlet temperature [°C]	CO inlet molar fraction [ppm]	HC inlet molar fraction [ppm]
1000	1.01	41.05	86.83	386	126
1000	1.00	38.89	108.74	343	159
1000	1.00	39.15	116.11	351	131
1000	1.00	38.72	124.39	317	157
1000	1.00	38.75	132.49	254	86
1000	1.01	38.64	159.60	270	137
1000	1.01	39.52	204.43	323	152
1000	1.01	40.29	254.16	473	164
1000	1.02	45.14	306.65	370	113
1250	1.01	51.63	200.02	402	205
1250	1.02	54.02	248.16	536	194
1250	1.03	62.23	305.23	570	141
1475	1.04	65.27	148.69	566	246
1500	1.02	66.00	98.17	649	282
1500	1.03	71.52	207.60	533	210
1500	1.04	76.29	253.22	595	190
1500	1.05	90.25	309.95	367	81

 doi:10.20944/preprints202405.0045.v1

Table A2. Input data for 2500 m & -7°C.

Engine speed [rpm]	OC inlet pressure [bar]	Exhaust gas mass flow [kg/h]	OC inlet temperature [°C]	CO inlet molar fraction [ppm]	HC inlet molar fraction [ppm]
1000	0.76	31.57	99.46	914	512
1000	0.76	33.02	128.13	495	262
1000	0.75	33.57	152.44	423	258
1000	0.76	33.25	180.81	274	196
1000	0.77	35.78	275.54	286	181
1250	0.75	39.49	94.32	1169	836
1250	0.75	42.71	158.14	548	322
1250	0.76	43.22	181.54	411	253
1250	0.76	44.23	220.36	294	221
1250	0.76	52.74	275.96	202	124
1500	0.75	54.22	92.52	1194	838
1500	0.76	58.72	147.59	616	257
1500	0.76	60.33	158.77	461	268
1500	0.76	65.58	207.22	308	175
1500	0.76	67.81	252.96	222	97
1500	0.77	75.07	301.61	198	78
1750	0.76	70.01	125.98	946	468
1750	0.78	72.21	172.99	602	290
1750	0.78	78.31	230.25	384	217
1750	0.78	81.23	278.57	257	154

Appendix B

This appendix includes Table A3 with the pre-exponential factors and activation energies of the reactions from Table 2 obtained in the model calibration.

Table A3. Calibration parameters.

Reaction	Pre-exponential factors [-]	Activation energy [kJ/mol]
1	$1.05 \cdot 10^{2}$	0
2	$2.98 \cdot 10^{12}$	101000
3	$2.48 \cdot 10^{15}$	84800
4	$7.31 \cdot 10^{14}$	92000
5	$6.55 \cdot 10^{7}$	41000
6	$9.67 \cdot 10^{6}$	45600
7	$6.09 \cdot 10^{14}$	78400
8	$6.09 \cdot 10^{14}$	78400
9	$5.00 \cdot 10^{10}$	60000
10	$1.01 \cdot 10^{8}$	81200
11	$1.1 \cdot 10^{15}$	71800
12	$5.96 \cdot 10^{13}$	71800
13	$3.80 \cdot 10^{9}$	88000
14	$4.6 \cdot 10^{8}$	107100
HC maximum capacity [mol/#]	$5.0 \cdot 10^{-5}$	
OH maximum capacity [mol/#]	$5.0 \cdot 10^{-5}$	

References

1. Claßen, J.; Pischinger, S.; Krysmon, S.; Sterlepper, S.; Dorscheidt, F.; Doucet, M.; Reuber, C.; Görgen, M.; Scharf, J.; Nijs, M.; et al. Statistically supported real driving emission calibration: Using cycle generation to provide vehicle-specific and statistically representative test scenarios for Euro 7. *International Journal of Engine Research* **2020**, *21*, 1783–1799. https://doi.org/10.1177/1468087420935221.

2. Ravi, S.S.; Osipov, S.; Turner, J.W. Impact of Modern Vehicular Technologies and Emission Regulations on Improving Global Air Quality. *Atmosphere* **2023**, *14*, 1164. https://doi.org/10.3390/atmos14071164.
3. Tang, G.; Wang, S.; Du, B.; Cui, L.; Huang, Y.; Xiao, W. Study on pollutant emission characteristics of different types of diesel vehicles during actual road cold start. *Science of The Total Environment* **2022**, *823*, 153598. https://doi.org/10.1016/j.scitotenv.2022.153598.
4. Shahariar, G.H.; Sajjad, M.; Suara, K.A.; Jahirul, M.; Chu-Van, T.; Ristovski, Z.; Brown, R.J.; Bodisco, T.A. On-road CO2 and NOx emissions of a diesel vehicle in urban traffic. *Transportation Research Part D: Transport and Environment* **2022**, *107*, 103326. https://doi.org/10.1016/j.trd.2022.103326.
5. Liu, J.; Li, Y.; Zhang, C.; Liu, Z. The effect of high altitude environment on diesel engine performance: Comparison of engine operations in Hangzhou, Kunming and Lhasa cities. *Chemosphere* **2022**, *309*, 136621. https://doi.org/10.1016/j.chemosphere.2022.136621.
6. Selleri, T.; Gioria, R.; Melas, A.D.; Giechaskiel, B.; Forloni, F.; Mendoza Villafuerte, P.; Demuynck, J.; Bosteels, D.; Wilkes, T.; Simons, O.; et al. Measuring Emissions from a Demonstrator Heavy-Duty Diesel Vehicle under Real-World Conditions—Moving Forward to Euro VII. *Catalysts* **2022**, *12*, 184. https://doi.org/10.3390/catal12020184.
7. Wang, Y.; Hao, C.; Ge, Y.; Hao, L.; Tan, J.; Wang, X.; Zhang, P.; Wang, Y.; Tian, W.; Lin, Z.; et al. Fuel consumption and emission performance from light-duty conventional/hybrid-electric vehicles over different cycles and real driving tests. *Fuel* **2020**, *278*, 118340. https://doi.org/10.1016/j.fuel.2020.118340.
8. EUR-Lex. Commission Regulation (EU) 2017/1151 of 1 June 2017 Supplementing Regulation (EC) No 715/2007 of the European Parliament and of the Council on Type-Approval of Motor Vehicles with Respect to Emissions from Light Passenger and Commercial Vehicles (Euro 5 and Euro 6) and on Access to Vehicle Repair and Maintenance Information, Amending Directive 2007/46/EC of the European Parliament and of the Council, Commission Regulation (EC) No 692/2008 and Commission Regulation (EU) No 1230/2012 and Repealing Commission Regulation (EC) No 692/2008., 2017. Accessed on February 14, 2024.
9. Commission, E. Questions and Answers: Commission proposal on the new Euro 7 standards. Available online:, 2022. Accessed on April 20, 2024.
10. Commission, E.; Directorate-General for Internal Market, Industry, E.; SMEs. *Technical studies for the development of Euro 7 – Testing, pollutants and emission limits*; Publications Office of the European Union, 2022. https://doi.org/10.2873/97170.
11. Liu, X.; Lara, R.; Dufresne, M.; Wu, L.; Zhang, X.; Wang, T.; Monge, M.; Reche, C.; Di Leo, A.; Lanzani, G.; et al. Variability of ambient air ammonia in urban Europe (Finland, France, Italy, Spain, and the UK). *Environment International* **2024**, p. 108519. https://doi.org/10.1016/j.envint.2024.108519.
12. Giechaskiel, B.; Valverde, V.; Kontses, A.; Suarez-Bertoa, R.; Selleri, T.; Melas, A.; Otura, M.; Ferrarese, C.; Martini, G.; Balazs, A.; et al. Effect of extreme temperatures and driving conditions on gaseous pollutants of a Euro 6d-Temp gasoline vehicle. *Atmosphere* **2021**, *12*, 1011. https://doi.org/10.3390/atmos12081011.
13. Luján, J.M.; Climent, H.; Ruiz, S.; Moratal, A. Influence of ambient temperature on diesel engine raw pollutants and fuel consumption in different driving cycles. *International Journal of Engine Research* **2019**, *20*, 877–888. https://doi.org/10.1177/1468087418792353.
14. Bermúdez, V.; Serrano, J.R.; Piqueras, P.; Gómez, J.; Bender, S. Analysis of the role of altitude on diesel engine performance and emissions using an atmosphere simulator. *International Journal of Engine Research* **2017**, *18*, 105–117. https://doi.org/10.1177/1468087416679569.
15. Suarez-Bertoa, R.; Valverde, V.; Pavlovic, J.; Clairotte, M.; Selleri, T.; Franco, V.; Kregar, Z.; Astorga, C. On-road emissions of Euro 6d-TEMP passenger cars on Alpine routes during the winter period. *Environmental Science: Atmospheres* **2021**, *1*, 125–139. https://doi.org/10.1039/D0EA00010H.
16. Serrano, J.R.; Piqueras, P.; Sanchis, E.J.; Diesel, B. Analysis of the driving altitude and ambient temperature impact on the conversion efficiency of oxidation catalysts. *Applied Sciences* **2021**, *11*, 1283. https://doi.org/ https://doi.org/10.3390/app11031283.
17. Voltz, S.E.; Morgan, C.R.; Liederman, D.; Jacob, S.M. Kinetic Study of Carbon Monoxide and Propylene Oxidation on Platinum Catalysts. *Industrial & Engineering Chemistry Product Research and Development* **1973**, *12*, 294–301. https://doi.org/10.1021/i360048a006.
18. Oh, S.H.; Cavendish, J.C. Transients of Monolithic Catalytic Converters: Response to Step Changes in Feedstream Temperature as Related to Controlling Automobile Emissions. *Industrial and Engineering Chemistry Product Research and Development* **1982**, *21*. https://doi.org/10.1021/i300005a006.

19. Datye, A.K.; Votsmeier, M. Opportunities and challenges in the development of advanced materials for emission control catalysts. *Nature Materials* **2021**, *20*, 1049–1059. https://doi.org/10.1038/s41563-020-00805-3.
20. Lefort, I.; Herreros, J.M.; Tsolakis, A. Reduction of Low Temperature Engine Pollutants by Understanding the Exhaust Species Interactions in a Diesel Oxidation Catalyst. *Environmental Science & Technology* **2014**, *48*, 2361–2367. https://doi.org/10.1021/es4051499.
21. Pan, Y.; Xu, L.; Huang, L.; He, W.; Li, H.; Wang, S.; Long, Z.; Sun, Z. Identification of active sites in Pt–Co bimetallic catalysts for CO oxidation. *ACS Applied Energy Materials* **2021**, *4*, 11151–11161. https://doi.org/10.1021/acsaem.1c02049.
22. Du, Y.; Zou, J.; Guo, Y.; Xu, X.; Chen, H.; Su, C.; Zeng, Z.; Li, L. A novel viewpoint on the surface adsorbed oxygen and the atom doping in the catalytic oxidation of toluene over low-Pt bimetal catalysts. *Applied Catalysis A: General* **2021**, *609*, 117913. https://doi.org/10.1016/j.apcata.2020.117913.
23. Acar, C.; Dincer, I. The potential role of hydrogen as a sustainable transportation fuel to combat global warming. *International Journal of Hydrogen Energy* **2020**, *45*, 3396–3406. https://doi.org/10.1016/j.ijhydene.2018.10.149.
24. Shadidi, B.; Najafi, G.; Yusaf, T. A review of hydrogen as a fuel in internal combustion engines. *Energies* **2021**, *14*, 6209. https://doi.org/10.3390/en14196209.
25. Hernández, J.J.; Cova-Bonillo, A.; Wu, H.; Barba, J.; Rodríguez-Fernández, J. Low temperature autoignition of diesel fuel under dual operation with hydrogen and hydrogen-carriers. *Energy Conversion and Management* **2022**, *258*, 115516. https://doi.org/10.1016/j.enconman.2022.115516.
26. Nag, S.; Sharma, P.; Gupta, A.; Dhar, A. Experimental study of engine performance and emissions for hydrogen diesel dual fuel engine with exhaust gas recirculation. *International Journal of Hydrogen Energy* **2019**, *44*, 12163–12175. https://doi.org/10.1016/j.ijhydene.2019.03.120.
27. Mhadeshwar, A.B.; Vlachos, D.G. Microkinetic modeling for water-promoted CO oxidation, water-gas shift, and preferential oxidation of CO on Pt. *Journal of Physical Chemistry B* **2004**, *108*. https://doi.org/10.1021/jp048698g.
28. Piqueras, P.; Pla, B.; Sanchis, E.J.; García, E. Control-Oriented Reduced-Order Modelling of Conversion Efficiency in Dual-Layer Washcoat Catalysts With Accumulation and Oxidation Functions. In Proceedings of the Internal Combustion Engine Division Fall Technical Conference. American Society of Mechanical Engineers, 2022, Vol. 86540, p. V001T04A001. https://doi.org/10.1115/1.4062815.
29. Desantes, J.M.; Galindo, J.; Payri, F.J.; Piqueras, P.; Serrano, J.R. Device for Atmosphere Conditioning for Testing Combustion Engines, and Associated Method and Use, 2015. Patent WO 2015/110683 A1.
30. Desantes, J.M.; Galindo, J.; Payri, F.J.; Piqueras, P.; Serrano, J.R. Device for Conditioning the Atmosphere in Test of Alternative Internal Combustion Engines, Method and Use of Said Device, 2016. Patent WO 2016/116642 A1,.
31. Piqueras, P.; de la Morena, J.; Sanchis, E.J.; Conde, C.; Herreros, J.M.; Tsolakis, A. Potential of H2-Assisted Light-Off of Oxidation Catalyst in H2-Diesel Dual-Fuel Engines. In Proceedings of the Internal Combustion Engine Division Fall Technical Conference. American Society of Mechanical Engineers, 2023, Vol. 87561, p. V001T05A001. https://doi.org/10.1115/ICEF2023-110095.
32. Herreros, J.M.; Gill, S.S.; Lefort, I.; Tsolakis, A.; Millington, P.; Moss, E. Enhancing the low temperature oxidation performance over a Pt and a Pt-Pd diesel oxidation catalyst. *Applied Catalysis B: Environmental* **2014**, *147*. https://doi.org/10.1016/j.apcatb.2013.10.013.
33. Martin, J.; Arnau, F.; Piqueras, P.; Auñon, A. Development of an Integrated Virtual Engine Model to Simulate New Standard Testing Cycles. 2018, Vol. 2018-April. https://doi.org/10.4271/2018-01-1413.
34. Piqueras, P.; Ruiz, M.J.; Herreros, J.M.; Tsolakis, A. Sensitivity of pollutants abatement in oxidation catalysts to the use of alternative fuels. *Fuel* **2021**, *297*. https://doi.org/10.1016/j.fuel.2021.120686.
35. Piqueras, P.; Ruiz, M.J.; Herreros, J.M.; Tsolakis, A. Influence of the cell geometry on the conversion efficiency of oxidation catalysts under real driving conditions. *Energy Conversion and Management* **2021**, *233*. https://doi.org/10.1016/j.enconman.2021.113888.
36. Kryl, D.; Kočí, P.; Kubíček, M.; Marek, M.; Maunula, T.; Härkönen, M. Catalytic converters for automobile diesel engines with adsorption of hydrocarbons on zeolites. 2005, Vol. 44. https://doi.org/10.1021/ie050249v.

 doi:10.20944/preprints202405.0045.v1

37. Bissett, E.J. An Asymptotic Solution for Washcoat Pore Diffusion in Catalytic Monoliths. *Emission Control Science and Technology* **2015**, *1*. https://doi.org/10.1007/s40825-015-0010-2.
38. Ratnakar, R.R.; Dadi, R.K.; Balakotaiah, V. Multi-scale reduced order models for transient simulation of multi-layered monolith reactors. *Chemical Engineering Journal* **2018**, *352*. https://doi.org/10.1016/j.cej.2018.04.053.
39. Gieshoff, J.; Schäfer-Sindlinger, A.; Spurk, P.; Van Den Tillaart, J.; Garr, G. Improved SCR Systems for Heavy Duty Applications, SAE. Technical report, Paper 2000-01-0189, 2000. https://doi.org/https://doi.org/10.4271/2000-01-0189.
40. Rhodes, C.; Hutchings, G.; Ward, A. Water-gas shift reaction: finding the mechanistic boundary. *Catalysis Today* **1995**, *23*, 43–58. https://doi.org/https://doi.org/10.1016/0920-5861(94)00135-O.
41. Lagarias, J.C.; Reeds, J.A.; Wright, M.H.; Wright, P.E. Convergence Properties of the Nelder–Mead Simplex Method in Low Dimensions. *SIAM Journal on Optimization* **1998**, *9*, 112–147. https://doi.org/10.1137/S1052623496303470.